Efficient iterative reconstruction with beam shape compensation for THz computed tomography

LARS-PAUL LUMBEECK,[1,*] PAVEL PARAMONOV,[1] JAN SIJBERS,[1] AND JAN DE BEENHOUWER[1]

[1]imec-Vision Lab, Dept. of Physics, University of Antwerp, Antwerp, Belgium

*lars-paul.lumbeeck@uantwerpen.be

Abstract: Terahertz (THz) computed tomography (CT) is an emerging nondestructive and non-ionizing imaging method. Most THz reconstruction methods rely on the Radon transform, originating from X-ray imaging, in which the X-rays propagate in straight lines. However, a THz beam has a finite width, and ignoring its shape results in blurred reconstructed images. Moreover, accounting for the THz beam model in a straightforward way in an iterative reconstruction method results in extreme demands in memory and in slow convergence. In this paper, we propose an efficient iterative reconstruction that incorporates the THz beam shape, while avoiding the above disadvantages. Both simulation and real experiments show that our approach results in improved resolution recovery in the reconstructed image. Furthermore, we propose a suitable preconditioner to improve the convergence speed of our reconstruction.

1   Introduction

THz imaging is a relatively recent field in imaging science with the first reported results dating back from 1995 [1]. It is a non-invasive, non-destructive and non-ionizing imaging technique with which the interior of objects can be visualized. THz imaging has a wide range of application domains, such as the study of biological materials (e.g., human breast tumors [2], human bones [3]), glass fibre-reinforced polymers [4], artwork, and ancient artefacts examination [5–7], as well as security and surveillance [8–10].

THz transmission imaging can be applied to perform tomography - a method, where, by combining multiple projection images acquired from different angles, the internal structure of a sample can be reconstructed. Most THz CT reconstruction methods are based on the Radon transform [11] to model the forward projection [12–16], in which it is assumed that radiation propagates on a straight path through samples. When imaging in the THz range, however, this assumption no longer holds, and wave-like effects such as refraction, reflection, diffraction and the THz beam shape will lower the image quality of the reconstructed images if they are not accounted for in the reconstruction algorithm.

A common way to account for refraction is through the application of ray tracing techniques in the implementation of the forward model. By simulating both the beam shape and beam steering with ray tracing, realistic simulation of projection artifacts can be achieved [17]. However, incorporating the THz beam model into a reconstruction algorithm remains a challenging task. It also has been shown that applying ray tracing to an a priory known set of interfaces, e.g., from a CAD model, can compensate for refraction and reflection losses, resulting in a significant improvement in the reconstruction quality [15, 18]. Another possibility of accounting for the effects of refraction is using nonlinear mathematical refraction models based on Maxwell's equations [19]. Without prior knowledge on the interfaces, incorporation of reflection and refraction losses in a reconstruction remains a challenging task. For soft materials, such as polyethylene foams, however, the beam shape plays a more dominant role in the reconstructed

45 image quality than refraction and reflection losses.

46 In the literature, different techniques were proposed for improving resolution and signal to
47 noise ratio of THz images [20–22]. An approach to the beam shape compensation in THz CT
48 reconstruction was described in [23]. There, authors proposed the modification of the Radon
49 transform that accounts for the beam shape by adding a convolution of the projected volume with
50 the THz beam model. To compensate for the projection blur in the reconstruction process, a
51 deconvolution with the beam shape of the back-projected images was proposed, which resulted
52 in improved sharpness of the reconstructed images. However, since in the forward projection
53 the sample is imaged with a beam of which the width changes as it passes through it, a simple
54 deconvolution cannot compensate for the varying width.

55 In this paper, we introduce a generic iterative reconstruction approach, into which the beam shape
56 can be incorporated. It requires both the THz forward projection operator and its adjoint, which
57 performs an additional convolution with the THz beam model in the back projection, instead of
58 the deconvolution. However, the system of linear equations in this case has two problems. Firstly,
59 the system matrix in such system is not sparse, which makes iterative reconstruction unfeasible
60 due to a large amount of memory needed to store it. Secondly, the system's high condition
61 number results in slow convergence rates (the condition number of a matrix measures how much
62 a small change in the input vector changes the solution of the system, making it a predictor for
63 convergence rates). In our work, we address both problems, by proposing an adaptation of the
64 system matrix to the THz forward projection model for which the iterative reconstruction methods
65 can be applied directly. Furthermore, we propose a preconditioner to increase convergence rates
66 and analyze its effect on the reconstruction. We show on both simulated and experimental THz
67 data that our reconstruction method results in improved resolution in the resulting images.

2 Methods and experiments

69 In this section, firstly, the derivation and reasoning behind our THz projection model are explained
70 in part 2.1. Then, we set the ground works for our iterative reconstruction methods, by discussing
71 the drawbacks of inverse techniques. This then leads into part 2.2, where the different iterative
72 methods are fleshed out. Finally, our simulated and real data experiments are discussed in part
73 2.3, as well as our experimental THz setup.

2.1 THz forward projection and its inverse

75 The Radon transform is defined as follows [24]:

$$R_\theta(\rho, h) = \iiint\limits_{-\infty}^{+\infty} \mu(x, y, z)\delta(\rho - x\cos\theta - y\sin\theta)\delta(z - h)dxdydz, \tag{1}$$

76 with μ the attenuation coefficient, θ the projection angle, and ρ and h the displacements of
77 the projection along the projection line and the z-axis respectively. In this model, the beam is
78 approximated by a line with zero width, which is a valid approximation if the wavelength of the
79 radiation is small compared to the size of the object. In THz imaging, this assumption no longer
80 holds, resulting in more blurry images when compared to X-ray projections. To minimize image
81 blur, the beam width must be taken into account in CT reconstructions [25].

82 The Radon transform can be derived from the Beer-Lambert law, which is in turn a solution of the
83 differential equation $dI(z) = -\mu(z)I(z)dz$ that describes the beam intensity loss as it propagates
84 in the z direction through matter with the attenuation coefficient μ :

$$T = e^{-\int_L \mu ds}, \tag{2}$$

85 with T the beam transmission, and L the path of the beam. A similar reasoning can be applied

for deriving the Beer-Lambert law that describes the propagation of the beam with a point spread function (PSF) $\Phi(x, y, z)$:

$$dI(z) = -\left\{ \iint \Phi(x, y, z)\mu(x, y, z)dxdy \right\} I(z)dz. \tag{3}$$

In Eq. (3), $\Phi(x, y, z)$ can be interpreted as weights of the attenuation coefficients computed in the plane perpendicular to the propagation direction. The solution to Eq. (3) is:

$$I(z) = I_0 e^{-\int_0^z \{ \iint \Phi(x,y,z')\mu(x,y,z')dxdy \}dz'}, \tag{4}$$

with I_0 the intensity measured without an object. This results in the following transmission T:

$$T = \frac{I}{I_0} = e^{-\int \Phi(x,y,z)\mu(x,y,z)dxdydz}. \tag{5}$$

Using Eq. (5), we construct a modified Radon transform for the beam propagating in the (x, y) plane:

$$p_\theta(\rho, h) = \iiint \Phi(\rho - x\cos\theta - y\sin\theta, -x\sin\theta + y\cos\theta, h - z)\mu(x, y, z)dxdydz, \tag{6}$$

which we further refer to as the THz Radon transform. Here, Φ_θ is the light distribution Φ translated and rotated in the same manner as the beam would be in the measurement. Eq. (6) can be rewritten as a 2D convolution, perpendicular to the propagation direction [23]:

$$p_\theta(\rho, h) = \iiint \mu * \Phi_\theta(x, y, z)\delta(h - z)\delta(\rho - x\cos\theta - y\sin\theta)dxdydz, \tag{7}$$

with $\Phi_\theta(x, y, z)$ the rotated beam PSF. The intensity profile of the beam in THz imaging is typically approximated with a Gaussian distribution [23]:

$$\Phi(x, y, z) = \frac{2}{\pi} \frac{1}{w^2(y)} e^{-\frac{2(x^2+z^2)}{w^2(y)}} \tag{8}$$

with y the axial distance from the beam focus. The function $w(y)$ represents the beam width and is given by:

$$w(y) = w_0\sqrt{1 + \left(\frac{y}{z_R}\right)^2} \tag{9}$$

with $w_0 = w(0)$ the beam waist's radius, z_R the Rayleigh range ($z_R = \frac{\pi w_0^2}{\lambda}$) and λ the wavelength of the beam. In the case $\mu(x, y, z)$ is constant in the z-direction, using the following definition:

$$\Phi^{2D}(x, y) = \int \Phi(x, y, z)dz = \sqrt{\frac{2}{\pi}} \frac{1}{w(y)} e^{-\frac{2x^2}{w^2(y)}}, \tag{10}$$

and rotating it over an angle θ:

$$\Phi_\theta^{2D}(x, y) = \sqrt{\frac{2}{\pi}} \frac{1}{w(-x\sin\theta + y\cos\theta)} e^{-\frac{2(x\cos\theta+y\sin\theta)^2}{w^2(-x\sin\theta+y\cos\theta)}}, \tag{11}$$

Eq. (7) turns into a 2D transform:

$$p_\theta(\rho) = \iint \mu * \Phi_\theta^{2D}(x, y)\delta(\rho - x\cos\theta - y\sin\theta)dxdy, \tag{12}$$

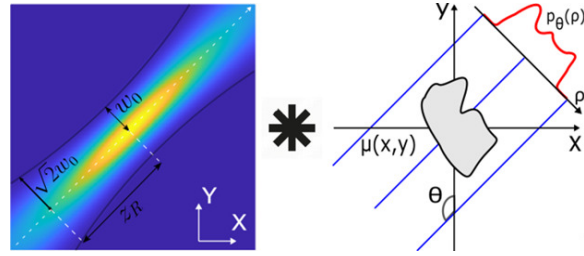Fig. 1.   Visualisation of the 2D THz Radon transform.The attenuation (right) is convolved with the beam profile (left), and subsequently projected over an angle θ.

with $*$ a 1D convolution perpendicular to the projection direction and Φ_θ^{2D} the intensity profile rotated over an angle of θ which defines the projection direction (Fig. 1). Now that a model for the forward projection is defined, it is possible to describe a reconstruction method able to recover the original attenuation image $\mu(x, y)$ back from the projections $p_\theta(\rho)$.

To create a fast reconstruction method, a possible inverse of the 2D THz Radon transform needs to be considered first. In the infinite Rayleigh length limit, the width of the beam becomes constant:

$$\lim_{z_R \to \infty} \Phi^{2D}(x, y) = \sqrt{\frac{2}{\pi}} \frac{1}{w_0} e^{-\frac{2x^2}{w_0^2}} = \Phi^{2D}(x, 0) = \Phi_0^{2D}. \tag{13}$$

Now that Φ_0^{2D} is independent of y, Eq. (12) can be inverted as follows (formula derivation can be found in Appendix A):

$$\mu(x, y) = \frac{1}{4\pi^2} \int_0^\pi \int_{-\infty}^{+\infty} |\omega| e^{i\omega(x\cos\theta + y\sin\theta)} \frac{\mathcal{F}[p_\theta(\rho)](\omega)}{\mathcal{F}[\Phi_0^{2D}](\omega)} d\omega d\theta, \tag{14}$$

where $\mathcal{F}[\cdot]$ represents the Fourier transform. Eq. (14) can be rewritten in the form of the inverse Radon transform, also known as the filtered back projection (FBP) [26]. In this case, $p_\theta(\rho)$ is first deconvolved with Φ_0^{2D}, resulting in $p_\theta'(\rho')$:

$$p_\theta'(\rho') = \frac{1}{2\pi} \int e^{i\rho'\nu} \frac{\int p_\theta(\rho) e^{-i\nu\rho} d\rho}{\int \Phi_0^{2D}(x') e^{-i\nu x'} dx'} d\nu \tag{15}$$

Then, FBP can be applied to reconstruct $\mu(x, y)$:

$$\mu(x, y) = \frac{1}{4\pi^2} \int_0^\pi \int_{-\infty}^{+\infty} |\omega| e^{i\omega(x\cos\theta + y\sin\theta)} \mathcal{F}[p_\theta'(\rho')](\omega) d\omega d\theta. \tag{16}$$

In practice, to achieve the highest possible resolution, the beam is focused on a sample, resulting in a finite value for z_R. In this case, Eq. (14) is not the inversion of Eq. (12). Although the inverse of Eq. (12) cannot be found, it is still possible to retrieve the transposed of Eq. (12) which corresponds to the back-projection operator of the system. The latter can be leveraged in an iterative reconstruction, allowing for z_R to be of arbitrary value. Hence we will resort to this type of reconstruction technique instead. Acquiring Eq. (16) was not in vain though, as it showcases a way of rearranging the forward projection into a combination of sparse matrices. This results in a dramatic reduction of memory consumption, and henceforth will be used in the next section when constructing the iterative reconstruction techniques."

2.2   Efficient iterative reconstruction

As for the conventional Radon transform, Eq. (12) can be rewriten as a system of linear equations:

$$\boldsymbol{p} = \boldsymbol{W}\boldsymbol{x}, \tag{17}$$

with p the vector of projection pixels, i.e., the discretized version of $p_\theta(\rho)$, W the system matrix and x the vector of image pixels, i.e., the discretized scalar field of the attenuation coefficient $\mu(x, y)$. However, unlike in the conventional forward projection model, the system matrix W is no longer sparse, which makes it unfeasible to store in the computer memory. Besides, the system in Eq. (17) has a high condition number, resulting in a low convergence rate. With the goal of solving the dense system matrix problem, we first prove that the transformation represented by W can be rewritten as a combination of three transformations: a convolution C with Φ_0^{2D}, the Radon transform W_R, and an additional correction matrix (H_x or H_p) applied to either the image pixels x, or to the projection pixels projected with the Radon transform W_R:

$$Wx = CW_R(H_x x) = CH_p(W_R x). \tag{18}$$

Splitting W into three sparse matrices greatly reduces the amount of memory needed for calculations. The system in Eq. (18) can be solved by any preferred iterative reconstruction. In this paper, we applied gradient descend with the step size γ_k chosen by the Barzilai–Borwein method [27]:

$$x^{k+1} = x^k + \gamma_k W^T \left(p - Wx^k\right). \tag{19}$$

Depending on how the correction matrix is defined, we describe two iterative solutions in the following sections.

2.2.1 Definition of the correction matrix

Applying the correction matrix H_x to the image pixels x results in the following linear system:

$$Wx = CW_R(H_x x) = p. \tag{20}$$

Let $h(x, y)$ be the solution in the constant beam limit, i.e., the result of FBP from Eq. (16), i.e., $h = H_x x$. The linear relation $h(x, y) = H_x \mu(x, y)$, with $H_x(\cdot)$ the transformation that links $h(x, y)$ and $\mu(x, y)$, can then be expressed as follows:

$$h(x, y) = \sqrt{\frac{2}{\pi}} \frac{z_R}{w_0} \iint\limits_{-\infty}^{+\infty} \delta(y'(y' - y) + x'(x' - x))e^{-\frac{2z_R^2(x-x')^2}{w_0^2 y'^2}} \mu(x', y')dx'dy'. \tag{21}$$

We will further refer the solution of the system in Eq. (20) as the *Reconstruction with Image Space Correction (RISC)*.

A second option for defining the system in Eq. (17) is by using the correction matrix H_p:

$$Wx = CH_p(W_R x) = p. \tag{22}$$

To derive H_p, we begin with rewriting Eq. (10) as follows:

$$\Phi^{2D}(x, y) = \int_{-\infty}^{+\infty} \int_{-\infty}^{+\infty} N_1(a)N_2(b)\delta(x - ay - b)dadb \tag{23}$$

with $N_1(a) = \frac{1}{\sqrt{2\pi}\sigma_a}e^{-\frac{a^2}{2\sigma_a^2}}$ and $N_2(b) = \frac{1}{\sqrt{2\pi}\sigma_b}e^{-\frac{b^2}{2\sigma_b^2}}$ two normal distributions. By setting $\sigma_a = \frac{w_0}{2z_R}$ and $\sigma_b = \frac{w_0}{2}$, $\Phi^{2D}(x, y)$ in Eq. (23) becomes equal to the one defined in Eq. (10). Hence, Eq. (7) can be rewritten as a sum of line integrals:

$$p_\theta(\rho) = \iint N_1(a)N_2(b)\frac{1}{\sqrt{a^2 + 1}}dadb \int_L \mu(\mathbf{r})ds \tag{24}$$

The path $\mathbf{r}(s)$ can be described by: $\mathbf{r}(s) = \left(s, \frac{a\sin\theta + \cos\theta}{a\cos\theta - \sin\theta}s - \frac{b + \rho}{a\cos\theta - \sin\theta}\right)$.

By defining $q_\varphi(t)$ as the Radon transform of $\mu(x, y)$:

$$q_\varphi(t) = \iint \mu(x, y)\delta\left(\cos(\varphi)x + \sin(\varphi)y - t\right) dxdy, \tag{25}$$

and applying $p'_\theta(\rho)$ from Eq. (15), Eq. (24) can be rewritten as follows:

$$p'_\theta = \int_{-\frac{\pm\pi}{2}}^{\frac{\pi}{2}} \int_{-\infty}^{+\infty} \frac{N_1(\tan(\theta - \varphi))}{|\cos(\theta - \varphi)|}\delta\left(t - \rho|\cos(\theta - \varphi)|\right) q_\varphi(t)dtd\varphi. \tag{26}$$

The transformation in Eq. (26) applied to $q_\varphi(t)$ defines the desired matrix $\boldsymbol{H}_p$. We will further refer the solution of the system in Eq. (22) as *Reconstruction with Sinogram Space Correction (RSSC)*.

2.2.2 Improving convergence by applying a preconditioner

To solve the problem of slow convergence of directly applied gradient descend to solve either Eq. (20) or Eq. (22), the inverted matrices $\boldsymbol{W}_R^{-1}$ and $\boldsymbol{C}^{-1}$ can be applied as preconditioners to the systems in Eq. (20) or Eq. (22). Applying $\boldsymbol{C}^{-1}$ as the preconditioner to Eq. (20) gives the following system of linear equations:

$$\boldsymbol{W}_R\boldsymbol{H}_x\boldsymbol{x} = \boldsymbol{C}^{-1}\boldsymbol{p}. \tag{27}$$

We will refer the solution of Eq. (27) as *RISC with preconditoner (RISC-P)*.

Applying $\boldsymbol{W}_R^{-1}\boldsymbol{C}^{-1}$ as the preconditioner to Eq. (20) is equivalent to first applying Eq. (16). In this case only $\boldsymbol{H}_x$ is needed for iterative reconstruction of $\boldsymbol{x}$, resulting in the following system:

$$\boldsymbol{H}_x\boldsymbol{x}=\boldsymbol{W}_R^{-1}\boldsymbol{C}^{-1}\boldsymbol{p} \tag{28}$$

The system in Eq. (28) demonstrated fast convergence, but severe artifacts in the resulting reconstructed image exclude it from further consideration [28].

$\boldsymbol{C}^{-1}$ can also be applied as the preconditioner to Eq. (22), resulting in the following system:

$$\boldsymbol{H}_p\boldsymbol{W}_R\boldsymbol{x}=\boldsymbol{C}^{-1}\boldsymbol{p}. \tag{29}$$

The solution of Eq. (29) will be referred as *RSSC with preconditoner (RSSC-P)*.

2.3 Experiments

2.3.1 Simulated CT data

To study the reconstruction quality and convergence speed of the proposed methods, two phantoms of size 200×200 pixels each were generated (see Fig. 2). The two phantoms are designed to uncover potential reconstruction artifacts. Both phantoms are binary images, with black corresponding to 0 and white - to 1. First, the 2D THz Radon transform was applied to both phantoms to generate the sinograms $p_\theta(\rho)$ with 250 angles spreading from 0 to 180 degrees. For the beam PSF, a Gaussian beam with frequency 500 GHz and $w_0 = 3$ mm was chosen. Next, the simulated sinograms were applied as input data for the conventional FBP, as well as for all four proposed iterative reconstruction methods from section 2.2. To quantify the reconstruction quality, the reconstructed images were compared to the original phantoms by applying two metrics: the mean squared error (MSE) and the structural similarity index measure (SSIM) [29]. The convergence of the proposed iterative reconstructions is studied by tracking the MSE value over a sufficiently high number of iterations.
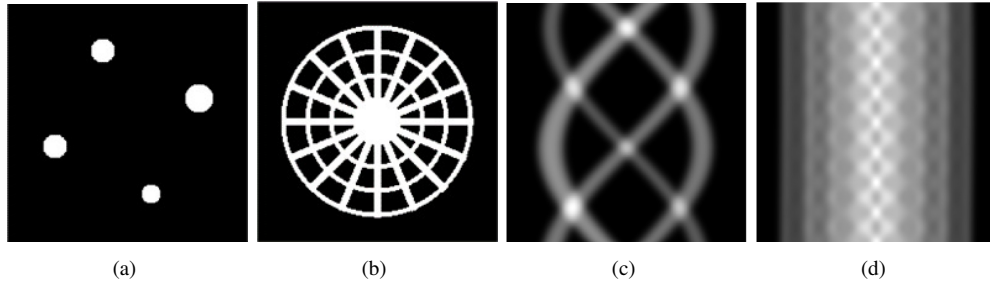
Fig. 2. (a-b) Simulated experiment phantoms, (c-d) and their 2D THz sinograms.
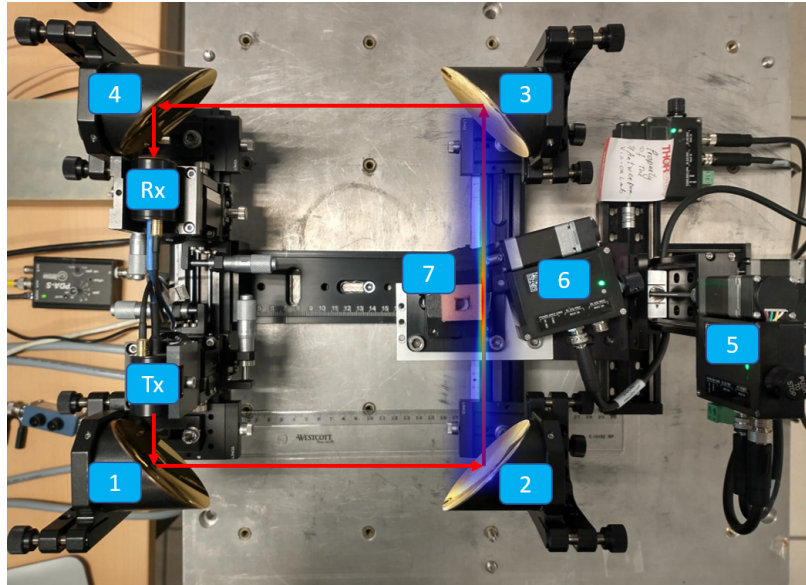

Fig. 3. THz CT system: Tx - THz transmitter, Rx - THz receiver, 1,3 - collimating mirrors, 2, 4 - focusing mirrors, 5 - XYZ-stage, 6 - rotation stage, 7 - foam sample.

2.3.2 Experimental setup for THz CT

All THz CT data was acquired with a THz set up suitable for raster scanning CT (see Fig. 3), based on the TeraScan 1550 Toptica system [30]. THz radiation is generated with two near-IR lasers and a photomixer based on an InGaAs photodiode. This is achieved by optical heterodyining two lasers into continuous wave (CW) THz radiation, exactly at the frequency difference of the lasers. Another InGaAs photomixer serves as a terahertz receiver, allowing for coherent lock-in detection of the photocurrent [30]. The resulting cone beam of THz light generated at the transmitter is focused on the sample to ensure the highest possible resolution. The transmitted light is then focused onto the receiver that represents a single pixel of the acquired image. The setup requires a combination of four precisely aligned off-axis parabolic mirrors that perform both collimation and focusing of the THz beam. In Fig. 3, the reflected focal length (RFL) for mirrors 1 and 4 is 2 inches, and 4 inches for mirrors 2 and 3. The three translation stages combined with the rotation stage enable us to perform CT acquisitions. The system is equipped with the Phase Modulation extension of Toptica [31] that allows for fast signal amplitude and phase retrieval for every pixel.

The photocurrent detected at the receiver is proportional to the THz field amplitude:

$$I_{Rx} \propto E_{THz} \cos\left(\frac{2\pi\nu}{c}\Delta L\right) = E_{THz} Re(e^{ik\Delta L}), \tag{30}$$

where c is the speed of light, ν is the THz frequency, $k = \frac{2\pi\nu}{c}$ the wave number, and ΔL is the optical path difference between the receiver and transmitter arms. In our setup, the phase of I_{Rx} is modulated with ΔL by changing the fiber arms in the fiber stretcher [31], allowing us to measure the amplitude and phase of I_{Rx} for every pixel.

Absorption and refraction can be taken into account simultaneously by defining a complex refractive index $\underline{n} = n + i\kappa$. In case the beam passes through a sample with a refractive index $\underline{n}$ for a distance d, the optical path difference is expected to change as follows:

$$\Delta L \rightarrow \Delta L - \int_d \underline{n}_{air} dz + \int_d \underline{n} dz \approx \Delta L - d + \int_d (n + i\kappa) dz, \tag{31}$$

where we assume $\underline{n}_{air} \approx 1$. Thus by adding the sample to the setup, the measured photocurrent is changed to:

$$I_{Rx} \propto E_{THz} Re(e^{ik(\Delta L - d)} e^{ik \int_d (n + i\kappa) dz}) = E_{THz} e^{-\frac{1}{2} \int_d \mu dz} \cos\left(k\Delta L + k \int_d (n - 1) dz\right), \tag{32}$$

where the known correlation $\mu = 2k\kappa$ between the attenuation coefficient μ and the imaginary part of refractive index κ was used [15]. Hence, the following transmission T and phase contrast $\Delta\Phi$ can be extracted for every pixel:

$$T = \left(\frac{E_{THz} e^{-\frac{1}{2} \int_d \mu dz}}{E_{THz}}\right)^2 = e^{-\int_d \mu dz}, \tag{33}$$

$$\Delta\Phi = k \int_d (n - 1) dz + m2\pi, \ \text{with } m \in \mathbb{Z}, \tag{34}$$

Note, that transmission in Eq. (33) matches the Beer-Lambert law, allowing us to compute the attenuation contrast. The refractive index can be retrieved from the phase contrast from Eq. (34). Applying the same logic as in section 2.1, the influence of the beam shape can be added to this model by approximating the path difference as follows:

$$\Delta L \rightarrow \Delta L - d + \int_d \left\{ \iint \Phi(x, y, z)(n(x, y, z) + i\kappa(x, y, z)) dx dy \right\} dz, \tag{35}$$

resulting in the following transmission and phase contrast:

$$T = e^{-\int \Phi(x,y)\mu(x,y)dxdy}$$
$$\Delta\Phi = k \int \Phi(x, y)(n(x, y) - 1) dx dy + m2\pi \qquad \text{with } m \in \mathbb{Z}, \tag{36}$$

Eq. (36) allows us to apply the iterative reconstruction methods described in 2.2.

2.3.3 THz data acquisition and processing

In this paper, we focus only on minimizing CT reconstruction artifacts caused by the THz beam shape, neglecting any other phenomena. However, reflections and refraction can be very strong in the THz domain for most dielectric materials, which makes the choice for a proper sample a
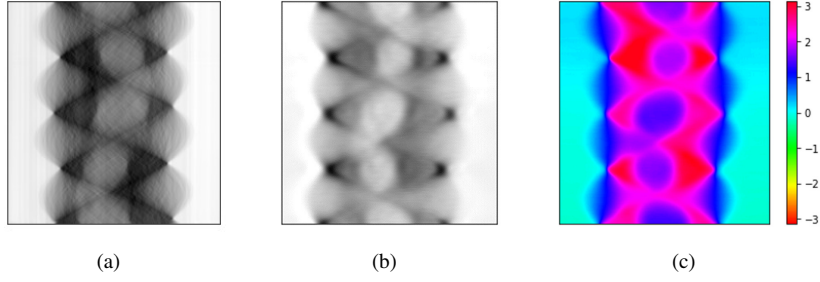
Fig. 4. 2D sinograms of the sample: (a) X-ray attenuation contrast, (b) THz attenuation contrast. (c) THz phase contrast.

challenging problem. Ideally, the sample should cause only beam attenuation, and no refraction at all. The tested sample for this work is made of polyethylene packaging foam, which has the desired properties, thanks to its low density. The sample has a cuboid shape with a side of ca. 20 mm and a through hole of ca. 7 mm. To acquire THz CT data of the sample, it was scanned in the THz system described in section 2.3.2 at 500 GHz, which corresponds to the wavelength of ca. 0.6 mm, resulting in 2D sinograms of the attenuation and phase contrast (Fig. 4). The beam width and Rayleigh length of the beam were determined to be equal to $w_0 = 3.34$ mm and $z_R = 58.50$ mm respectively for these measurements.

To validate and test our reconstruction algorithms, we compare results of iterative THz reconstructions with the reference 2D reconstruction of the sample, which was extracted from a high resolution 3D X-ray image acquired in a FleXCT system [32] (see Fig. 5a). To this end, a weighted average $\mu(x, y)$ of the 3D image $\mu_{3D}(x, y, z)$ along the vertical direction was computed, with weights that correspond to a Gaussian beam profile at the focal point (Fig. 5c):

$$\mu(x, y) = \int_{-\infty}^{\infty} \sqrt{\frac{2}{\pi w_0}} e^{-2\frac{(z-z_{fp})^2}{w_0^2}} \mu_{3D}(x, y, z) dz \tag{37}$$

with z_{fp} the z-coordinate of the focal point. The resulting 2D reference image of $\mu(x, y)$ is shown in Fig. 5f.

3   Results and discussion

3.1   Simulated data

The qualitative results of all proposed reconstructions are shown in Fig. 6 for the circles phantom, and in Fig. 7 for the spider web phantom. For both phantoms, the gradient descent was performed for 3000 iterations to output the final image. The quantitative comparison of the reconstructions in Fig. 6 and Fig. 7 is presented in Table 1.

A noticeable aspect when comparing the two reconstruction options *RISC* and *RSSC* is the appearance of a black spot in the center of the image for *RISC* and *RISC-P*. This is caused by the approximations made by discretizing H_x, which is not present in *RSSC*. The discretization H_p does not cause such artifacts (Fig. 7) and thus *RSSC-P* result in better reconstruction. The difference between *RISC* and *RSSC* is small, in terms of the mean squared error and SSIM, but *RSSC* removes the centre artifact, resulting in a straight upgrade compared to *RISC*. We conclude that *RSSC-P* is the method of choice for fast accurate reconstruction.

To quantify the convergence rates, the condition numbers were calculated for *RISC* and *RISC-P* for x of size $50 \times 50 \times 50$, which a forward projection of the 50×50 pixels image and with 50 projection angles. The condition numbers $\kappa_{RISC} = 4.4 \cdot 10^{17}$ and $\kappa_{RISC-P} = 2.0 \cdot 10^{10}$ clearly demonstrate the advantage of applying the preconditioner in *RISC-P*. In Fig. 8, the convergence
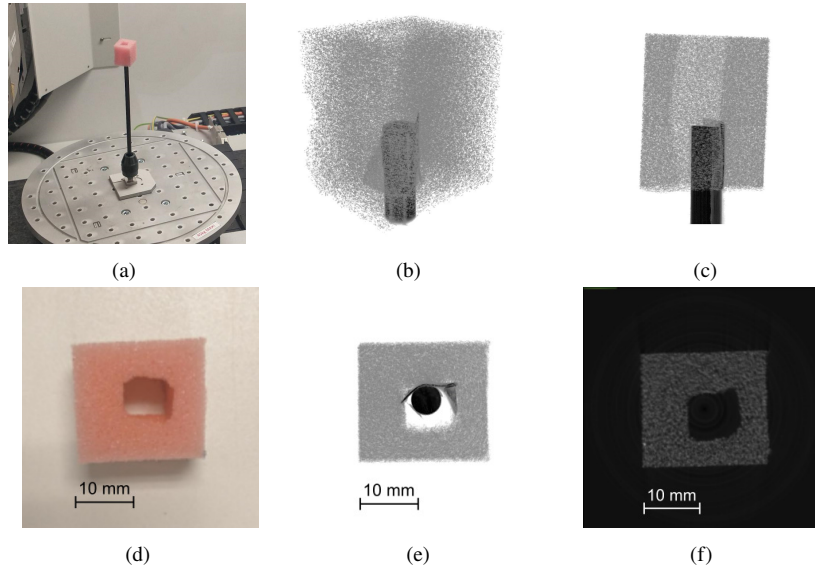
Fig. 5. (a) Experimental sample inside the FleXCT system and (d) its top view, (b) X-ray 3D image of the sample in the isometric view and (e) top view, (c) side view of the 3D X-ray image with the visualisation of weighted summation (red), (f) and the reference 2D X-ray reconstruction.
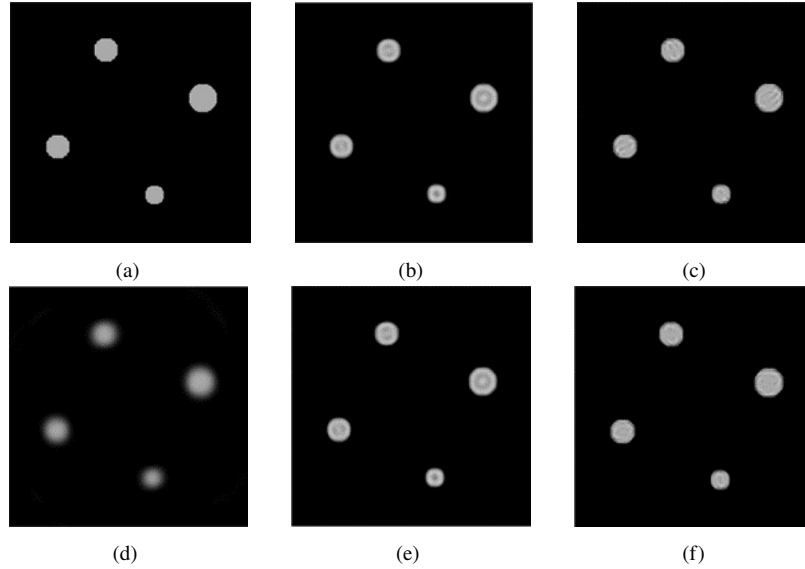

Fig. 6. (a) Circles phantom, and its reconstructions with (d) conventional FBP, (b) *RISC* and (c) *RISC-P*, (e), *RSSC*, (f), *RSSC-P*.

rate of the MSE is compared for the proposed gradient descent reconstructions. Using the preconditioner results in faster convergence for both systems *RISC-P* and *RSSC-P*, compared to their non-preconditioner versions. However, after executing gradient descent long enough for the non-preconditioner systems, the reconstructed images can be of a slightly higher quality than the ones reconstructed using their preconditioner versions Fig. 8b. So while *RISC* and *RSSC* have a
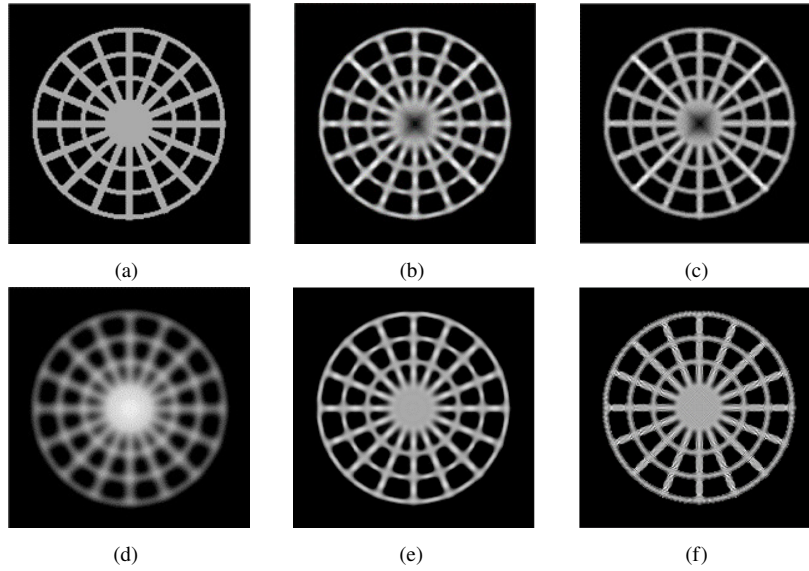
Fig. 7. (a) Spider web phantom, and its reconstructions with (d) conventional FBP, (b) *RISC* and (c) *RISC-P*, (e), *RSSC*, (f), *RSSC-P*.
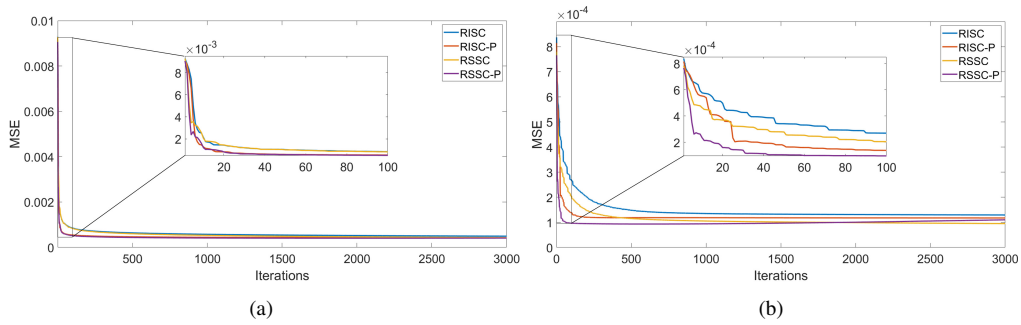

Fig. 8. The MSE in function of the iterations for (a) circles phantom and (b) spider web phantom

slow convergence rate, because the inverted transformations never need to be approximated, they do give the most accurate results over a relatively high number of iterations.

3.2 THz CT data

Both attenuation and phase contrast sinograms were first reconstructed with Barzilai–Borwein gradient descent with the conventional 2D Radon transform as a forward projection model (see Fig.9a,b). Since the reconstruction from the attenuation contrast sinogram resulted in a significantly lower quality compared to the phase contrast reconstruction, we further focused on only the phase contrast reconstruction. This data was then applied as an input for the different gradient descent-based (Barzilai–Borwein method [27]) reconstruction techniques: *RSSC*, *RSSC-P*, and a conventional (no beam compensation) CT method (Fig. 9). The conventional CT method is referred to as "Conventional GD" in Fig. 10.

To compare quantitatively using the X-ray reference image as the ground truth, the reference image was first transformed to match each reconstruction's orientation, position and scale. Applying

Method	Circles		Spider web	
	MSE, $\times 10^{-4}$	SSIM	MSE, $\times 10^{-4}$	SSIM
FBP	93.53	0.9332	9.46	0.5157
RISC	3.37	0.9749	1.48	0.8235
RISC-P	4.65	0.9831	1.19	0.8606
RSSC	6.00	0.9744	1.15	0.8608
RSSC-P	4.32	0.9831	0.93	0.8817

Table 1. Comparison of reconstructions on simulated data. For all iterative reconstructions, the gradient descent was performed for 500 iterations.

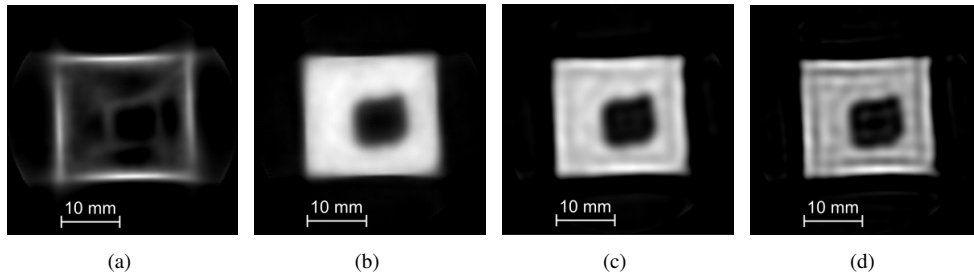(a)   (b)   (c)   (d)

Fig. 9. (a) Iterative reconstruction of the attenuation contrast without beam shape compensation, (b) iterative reconstruction of the phase contrast without beam shape compensation, reconstruction of the phase contrast with (c) *RSSC*, and (d) *RSSC-P*. For all reconstructions, the gradient descent was performed for 3000 iterations.

Method	MSE	SSIM
Conventional method	$4.0 \cdot 10^{-6}$	0.9951
RSSC	$2.1 \cdot 10^{-6}$	0.9978
RSSC-P	$2.8 \cdot 10^{-6}$	0.9973

Table 2. Reconstruction quality of the phase contrast reconstructions after 50 iterations.

these affine transformations, the pixel values were mapped to the ones from the THz phase shift reconstruction. To evaluate the accuracy of our reconstruction methods the MSE and SSIM of each image are compared after 50 iterations (Table 2). The reconstruction progress of the different reconstruction methods is visible in Fig. 10, where the MSE is plotted in function of the iteration count.

Our system does not take reflection and refraction losses into effect, which then will be wrongly interpreted as attenuation losses by the reconstruction algorithm. This explains the high attenuation prediction at the edges of the reconstruction. The refraction reconstruction is less effected by this phenomenon, because it is derived from phase contrast, not intensity loss.

Comparing the different reconstruction methods on the phase contrast sinogram, it is clear that both beam compensation methods greatly improve the MSE and SSIM. In Fig. 10 it is clear that *RSSC-P* indeed converges more quickly compared to *RSSC*. It quickly loses its edge though
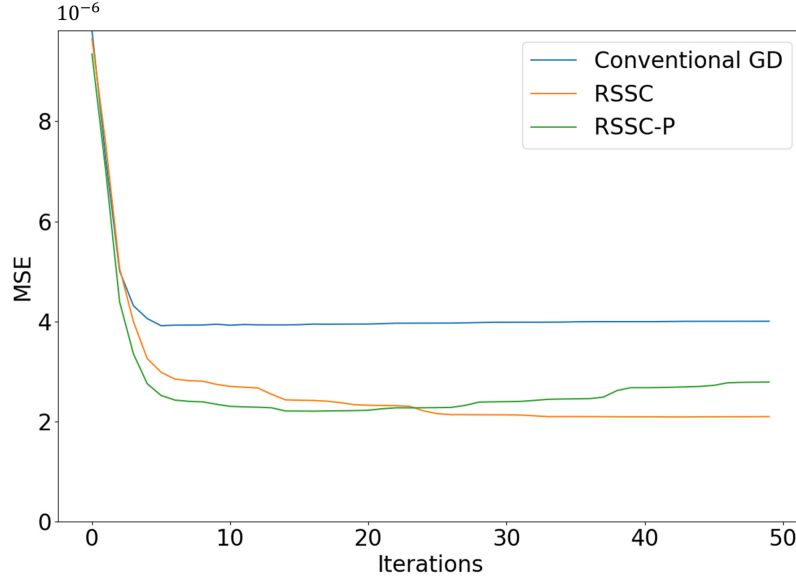
Fig. 10. The MSE in function of the iteration count of the three gradient descent (GD) iterative reconstructions. Conventional GD refers to a gradient descent without beam shape compensation.

because of overfitting, which can be mitigated by regularization. This means that the best results are achieved by *RSSC*, which is also shown by comparing the SSIM at 50 iterations The MSE and SSIM values in case of reconstruction from experimental data over 50 iterations is noticeably smaller than for the reconstruction from simulated data over 500 iterations. This discrepancy can be explained by the fact that the simulated tests were applied to discrete phantoms.

4 Conclusion

In this paper, a generic iterative reconstruction approach, into which the beam shape can be incorporated, was introduced. It is based on a modified version of the Radon transform in which the projected volume is convolved with the beam point spread function. Unfortunately, introducing the system matrix representing this modified version of the Radon transform, demands an extreme amount of memory and results in slow convergence. To address the extreme memory consumption caused by the system matrix density, we proposed splitting it into three sparse matrices, representing the convolution with the constant beam, conventional Radon transform, and an additional correction operator. The split can be done in two ways, depending on whether the correction is applied in the image space, or the projection space. We described both options, and by applying a preconditioner, we managed to increase the convergence rates of the corresponding iterative reconstructions.

The quality of the images reconstructed by the proposed methods was studied on both simulated and THz data, as well as the effects of applying the preconditioner on the reconstruction quality and convergence speed. The experiment on simulated data demonstrated improved sharpness in the reconstructed images. To validate and test our reconstruction algorithms on the THz data, measurements taken by a FleXCT system were considered as the ground truth. With the use of a THz set up, based on the TeraScan 1550 Toptica system, 2D sinograms of both attenuation and phase contrasts of a sample made of polyethylene foam were acquired. The

latter of which, was then utilized in iterative reconstructions. Compensating for the beam shape, by applying our proposed reconstruction methods to the phase contrast sinogram, resulted in improved reconstruction accuracy both for MSE and SSIM. Applying the preconditioner to the THz data reconstruction, resulted in worse image quality, which, looking at the convergence rate, is clearly caused by overfitting. The reconstruction methods proposed in this paper are not limited to THz, but can be applied to any type of wide beam measurement.

Funding

Acknowledgments

Disclosures

The authors declare no conflicts of interest.

Data Availability

Data underlying the results presented in this paper are not publicly available at this time but may be obtained from the authors upon reasonable request.

Appendix A   Derivation of the 2D THz Radon transform inversion

For the constant beam case, Eq. (12) becomes:

$$p_\theta(\rho) = \iint \mu * \Phi_\theta^{2D}(x, 0)\delta(\rho - x\cos\theta - y\sin\theta)dxdy. \tag{38}$$

This can then can be rewritten in the parameterized form:

$$p_\theta(\rho) = \iint \mu(x\cos\theta - y\sin\theta, x\sin\theta + y\cos\theta)\Phi_0^{2D}(\rho - x)dxdy, \tag{39}$$

and after applying the Fourier transform:

$$\mathcal{F}[p_\theta(\rho)](\omega) = \iint \left(\int e^{-i\rho\omega}\mu(x\cos\theta - y\sin\theta, x\sin\theta + y\cos\theta)\Phi_0^{2D}(\rho - x)d\rho \right) dxdy$$
$$= \int \left(\int e^{-ix\omega}\mu(x\cos\theta - y\sin\theta, x\sin\theta + y\cos\theta)dx \right) \mathcal{F}[\Phi_0^{2D}(\rho)](\omega)dy. \tag{40}$$

The Fourier transform $\mathcal{F}[\Phi_0^{2D}](\omega)$, which is independent of the dummy variables x and y, can be brought to the left side of the equal sign:

$$\frac{\mathcal{F}[p_\theta(\rho)](\omega)}{\mathcal{F}[\Phi_0^{2D}](\omega)} = \iint e^{-ix\omega} \mu(x\cos\theta - y\sin\theta, x\sin\theta + y\cos\theta)dxdy$$
$$= \iint e^{-i(x\cos\theta + y\sin\theta)\omega} \mu(x,y)dxdy. \tag{41}$$

Now it can easily be proven, that Eq. (14), indeed results in a formula for $\mu(x, y)$:

$$\int_0^\pi \int_{-\infty}^{+\infty} \frac{|\omega|}{4\pi^2} e^{i\omega(x'\cos\theta + y'\sin\theta)} \frac{\mathcal{F}[p_\theta(\rho)](\omega)}{\mathcal{F}[\Phi_0^{2D}](\omega)} d\omega d\theta$$
$$= \frac{1}{4\pi^2} \int_0^\pi \int_{-\infty}^{+\infty} \left(\iint |\omega| \mu e^{-i(x-x')\omega\cos\theta + (y-y')\sin\omega\theta} dxdy \right) d\omega d\theta. \tag{42}$$

As a last step, we substitute $\eta = \omega\cos\theta$ and $\zeta = \omega\sin\theta$:

$$\int_0^\pi \int_{-\infty}^{+\infty} \frac{|\omega|}{4\pi^2} e^{i\omega(x'\cos\theta + y'\sin\theta)} \frac{\mathcal{F}[p_\theta(\rho)](\omega)}{\mathcal{F}[\Phi_0^{2D}](\omega)} d\omega d\theta$$
$$= \frac{1}{4\pi^2} \iint \left(\iint \mu e^{-i(x-x')\eta + (y-y')\zeta} dxdy \right) d\eta d\zeta = \mu(x', y'), \tag{43}$$

References

1. B. B. Hu and M. C. Nuss, "Imaging with terahertz waves," Opt. letters **20**, 1716–1718 (1995).
2. A. J. Fitzgerald, V. P. Wallace, M. Jimenez-Linan, L. Bobrow, R. J. Pye, A. D. Purushotham, and D. D. Arnone, "Terahertz pulsed imaging of human breast tumors," Radiology **239**, 533–540 (2006).
3. M. Bessou, B. Chassagne, J.-P. Caumes, C. Pradère, P. Maire, M. Tondusson, and E. Abraham, "Three-dimensional terahertz computed tomography of human bones," Appl. optics **51**, 6738–6744 (2012).
4. J. Wang, J. Zhang, T. Chang, L. Liu, and H.-L. Cui, "Terahertz nondestructive imaging for foreign object detection in glass fibre-reinforced polymer composite panels," Infrared Phys. & Technol. **98**, 36–44 (2019).
5. J. Labaune, J. Jackson, S. Pagès-Camagna, M. Menu, and G. Mourou, "Terahertz investigation of egyptian artifacts," in *35th International Conference on Infrared, Millimeter, and Terahertz Waves,* (IEEE, 2010), pp. 1–3.
6. J.-P. Caumes, A. Younus, S. Salort, B. Chassagne, B. Recur, A. Ziéglé, A. Dautant, and E. Abraham, "Terahertz tomographic imaging of xviiith dynasty egyptian sealed pottery," Appl. optics **50**, 3604–3608 (2011).
7. J. B. Jackson, J. Bowen, G. Walker, J. Labaune, G. Mourou, M. Menu, and K. Fukunaga, "A survey of terahertz applications in cultural heritage conservation science," IEEE Trans. on Terahertz Sci. Technol. **1**, 220–231 (2011).
8. H. Quast and T. Loffler, "3d-terahertz-tomography for material inspection and security," in *2009 34th International Conference on Infrared, Millimeter, and Terahertz Waves,* (IEEE, 2009), pp. 1–2.
9. P. C. Theofanopoulos and G. C. Trichopoulos, "A novel thz radar imaging system using the radon transform," in *2017 IEEE International Symposium on Antennas and Propagation & USNC/URSI National Radio Science Meeting,* (IEEE, 2017), pp. 1513–1514.
10. P. C. Theofanopoulos, M. Sakr, and G. C. Trichopoulos, "Multistatic terahertz imaging using the radon transform," IEEE Trans. on Antennas Propag. **67**, 2700–2709 (2019).
11. J. Radon, "Uber die bestimmug von funktionen durch ihre integralwerte laengs geweisser mannigfaltigkeiten," Berichte Saechsishe Acad. Wissenschaft. Math. Phys., Klass **69**, 262 (1917).
12. W.-T. Su, Y.-C. Hung, P.-J. Yu, C.-W. Lin, and S.-H. Yang, "Physics-guided terahertz computational imaging," arXiv preprint arXiv:2205.00327 (2022).
13. M. Suga, Y. Sasaki, T. Sasahara, T. Yuasa, and C. Otani, "Phase contrast computed tomography using continuous thz source," in *2017 25th European Signal Processing Conference (EUSIPCO),* (IEEE, 2017), pp. 1510–1513.
14. F. Zhong, L. Niu, W. Wu, and F. Liu, "Dictionary learning-based image reconstruction for terahertz computed tomography," J. Infrared, Millimeter, Terahertz Waves **42**, 829–842 (2021).
15. J. Tepe, T. Schuster, and B. Littau, "A modified algebraic reconstruction technique taking refraction into account with an application in terahertz tomography," Inverse Probl. Sci. Eng. **25**, 1448–1473 (2017).
16. A. Roggenbuck, H. Schmitz, A. Deninger, I. C. Mayorga, J. Hemberger, R. Güsten, and M. Grüninger, "Coherent broadband continuous-wave terahertz spectroscopy on solid-state samples," New J. Phys. **12**, 043017 (2010).
17. P. Paramonov, L.-P. Lumbeeck, J. De Beenhouwer, and J. Sijbers, "Accurate terahertz imaging simulation with ray tracing incorporating beam shape and refraction," in *2020 IEEE International Conference on Image Processing (ICIP),* (IEEE, 2020), pp. 3035–3039.
18. P. Fosodeder, S. van Frank, and C. Rankl, "Highly accurate thz-ct including refraction effects," Opt. Express **30**, 3684–3699 (2022).

19. S. Hubmer, A. Ploier, R. Ramlau, P. Fosodeder, and S. van Frank, "A mathematical approach towards thz tomography for non-destructive imaging," arXiv preprint arXiv:2010.14938 (2020).

20. M. Ljubenović, S. Bazrafkan, P. Paramonov, J. D. Beenhouwer, and J. Sijbers, "Cnn-based deblurring of thz time-domain images," Commun. Comput. Inf. Sci. **1474 CCIS**, 477 – 494 (2022).

21. M. Ljubenović, L. Zhuang, J. De Beenhouwer, and J. Sijbers, "Joint deblurring and denoising of thz time-domain images," IEEE Access **9**, 162–176 (2020).

22. K. Ahi, "A method and system for enhancing the resolution of terahertz imaging," Measurement **138**, 614–619 (2019).

23. B. Recur, J.-P. Guillet, I. Manek-Hönninger, J.-C. Delagnes, W. Benharbone, P. Desbarats, J.-P. Domenger, L. Canioni, and P. Mounaix, "Propagation beam consideration for 3d thz computed tomography," Opt. express **20**, 5817–5829 (2012).

24. M. D'Acunto, A. Benassi, D. Moroni, and O. Salvetti, "3D image reconstruction using Radon transform," Signal, Image Video Process. **10**, 1 – 8 (2016).

25. J. Guillet, B. Recur, I. Manek-Hönninger, J. Delagnes, W. Benharbone, P. Desbarats, J. Domenger, L. Canioni, and P. Mounaix, "3d-terahertz tomography using a more realistic beam propagation model applied to different image reconstruction methods," in *2012 37th International Conference on Infrared, Millimeter, and Terahertz Waves,* (IEEE, 2012), pp. 1–2.

26. G. T. Herman, "Image reconstruction from projections," The fundamental computerized tomography pp. 260–276 (1980).

27. J. Barzilai and J. M. Borwein, "Two-point step size gradient methods," IMA journal numerical analysis **8**, 141–148 (1988).

28. L.-P. Lumbeeck, P. Paramonov, J. Sijbers, and J. De Beenhouwer, "The radon transform for terahertz computed tomography incorporating the beam shape," in *2020 IEEE International Conference on Image Processing (ICIP),* (IEEE, 2020), pp. 3040–3044.

29. Z. Wang, A. C. Bovik, H. R. Sheikh, and E. P. Simoncelli, "Image quality assessment: from error visibility to structural similarity," IEEE transactions on image processing **13**, 600–612 (2004).

30. Toptica, "Toptica: Terascan specifications," https://www.toptica.com/products/terahertz-systems/frequency-domain/terascan.

31. A. Roggenbuck, K. Thirunavukkuarasu, H. Schmitz, J. Marx, A. Deninger, I. C. Mayorga, R. Güsten, J. Hemberger, and M. Grüninger, "Using a fiber stretcher as a fast phase modulator in a continuous wave terahertz spectrometer," J. Opt. Soc. Am. B: Opt. Phys. **29**, 614 – 620 (2012).

32. B. D. Samber, J. Renders, T. Elberfeld, Y. Maris, J. Sanctorum, N. Six, Z. Liang, J. D. Beenhouwer, and J. Sijbers, "Flexct: a flexible x-ray ct scanner with 10 degrees of freedom," Opt. Express **29**, 3438–3457 (2021).